UC Merced

UC Merced Previously Published Works

Title

Magnetic field weakening carrier secondary recombination in/on amorphous Co0.07Fe0.93Ox co-catalysts to boost BiVO4/Co0.07Fe0.93Ox film photoanodes for solar water splitting

Permalink

https://escholarship.org/uc/item/2zf7293h

Journal

Electrochimica Acta, 572

ISSN

0013-4686

Authors

Huang, Yujie

Du, Jinyan

Jin, Xianchun

et al.

Publication Date

2026-10-01

DOI

10.1016/j.electacta.2026.149211

Peer reviewed

eScholarship.org Powered by the California Digital Library
University of California

Electrochimica Acta 572 (2026) 149211

Contents lists available at ScienceDirect

Electrochimica Acta

journal homepage: www.journals.elsevier.com/electrochimica-acta

Magnetic field weakening carrier secondary recombination in/on amorphous $Co_{0.07}Fe_{0.93}O_x$ co-catalysts to boost $BiVO_4/Co_{0.07}Fe_{0.93}O_x$ film photoanodes for solar water splitting

Yujie Huang [a,1], Jinyan Du [a,b,1], Xianchun Jin [c], Jiahe Li [a], Lingling Liao [a], Tao Han [a], Gaili Ke [a,*], Huichao He [a,*]

[a] College of Materials and New Energy, Chongqing University of Science and Technology, Chongqing 401331, China
[b] School of Chemistry, University of Glasgow, Glasgow G12 8QQ, United Kingdom
[c] School of Physics, University of Electronic Science and Technology of China, Chengdu 611731, China

ARTICLE INFO

Keywords:
$BiVO_4$
Solar water oxidation
Amorphous co-catalysis
Magnetic field
Carrier secondary recombination

ABSTRACT

Amorphous co-catalysts/$BiVO_4$ photoanodes could achieve high-activity solar water oxidation, but the amorphous co-catalysts usually lack selectivity for electrons/holes extraction from $BiVO_4$ and exist carrier secondary recombination accordingly. Herein, amorphous $Co_{0.07}Fe_{0.93}O_x$ nanoparticles with magnetic property were coupled on $BiVO_4$ film to form $BiVO_4/Co_{0.07}Fe_{0.93}O_x$ (BVO/CFO) film photoanode for solar water oxidation under magnetic field. In magnetic field-free condition, the BVO/CFO film photoanode had higher solar water oxidation activity (2.380 mA/cm^2 at 1.23 V *vs.* RHE) than BVO film photoanode (1.205 mA/cm^2 at 1.23 V *vs.* RHE), due to the presence of CFO co-catalysis. Under an external magnetic field of 8 mT, the solar water oxidation activity of BVO film photoanode was increased by 2.98% through magnetic field weakening the nonradiative recombination of carrier, relative to it in magnetic field-free condition. By comparison, the activity of BVO/CFO film photoanode for solar water oxidation under same magnetic field was improved by 29.83% (2.380 mA/cm^2 to 3.090 mA/cm^2 at 1.23 V *vs.* RHE), which was 10 times to the improvment on BVO film photoanode. In addition, the BVO/CFO film photoanode had more stable activity during continuous solar water oxidation than BVO film photoanode under magnetic field. Mechanism investigations revealed that magnetic field can significantly reduce the carrier secondary recombination in/on amorphous magnetic CFO co-catalysts to boost BVO/CFO film photoanode for solar water oxidation, but not change the reaction kinetics obviously.

1. Introduction

With the gradual deterioration of climate environment and the potential shortage of fossil energy, photoelectrochemical (PEC) water splitting that be driven by active semiconductor photoelectrodes provides a feasible approach for green H_2 fuel production using solar energy [1–3]. Since its suitable band structure ($E_g \approx 2.5$ eV, $E_{valence\ band} \approx 2.4$ V *vs.* RHE) enables to capture ~9.3% solar light to initiate water oxidation, $BiVO_4$ has been considered as a promising photoanode material for solar water splitting [4–7]. In principle, solar water oxidation on $BiVO_4$ photoanode is initiated by the photogenerated holes of $BiVO_4$, thereby manipulating carrier separation and transfer in/on $BiVO_4$ for water oxidation is extremely important. In our previous work, it has been found that the introduction of magnetic field at the side of photoanodes and photocathodes can improve their water solar splitting activity through weakening the nonradiative recombination of carrier [8]. Unfortunately, the solar water splitting activity improving on photoelectrodes under magnetic field is not high enough, since the activity of pristine semiconductor photoelectrodes is limited. For the sake of achieving solar water splitting efficiently, $BiVO_4$ photoanodes are usually coupled with co-catalysts to modify the carrier separation and transfer as well as water oxidation kinetics [9–17]. To fully unleash the potential of magnetic field for improving solar water splitting on photoanode systems, it is necessary to take co-catalysts/$BiVO_4$ photoanode as typical model to study the effect of magnetic field.

$BiVO_4$ photoanodes coupling with amorphous co-catalysts (such as,

* Corresponding authors.
E-mail addresses: kegaili@cqust.edu.cn (G. Ke), hehuichao@cqust.edu.cn (H. He).
[1] These authors contributed equally to this work.

https://doi.org/10.1016/j.electacta.2026.149211
Received 10 April 2026; Received in revised form 13 May 2026; Accepted 27 May 2026
Available online 28 May 2026
0013-4686/© 2026 Elsevier Ltd. All rights are reserved, including those for text and data mining, AI training, and similar technologies.

CoPi, FeOOH) have been demonstrated to achieve carrier transfer to co-catalysts in thermodynamics as well as accelerate water oxidation in kinetics [9–20]. Significantly, amorphous co-catalysts usually lack selectivity for electrons/holes extraction from $BiVO_4$, which could result in carrier secondary recombination in/on amorphous co-catalysts after $BiVO_4$'s carrier transferring through amorphous co-catalysts/$BiVO_4$ interfaces [12]. Therefore, minimizing the carrier secondary recombination in/on amorphous co-catalysts could achieve solar water oxidation on co-catalysts/$BiVO_4$ photoanodes efficiently. In recent years, the introduction of magnetic field has emerged as an effective approach to enhance the activity of magnetic catalysts for oxygen evolution reaction [21–26]. Typically, Xu et al. found that the spin exchange between ferromagnetic $CoFe_2O_4$ and adsorbed oxygen species in the first electron transfer step of oxygen evolution reaction could be turned to be coherent and fast under a constant magnetic field, thereby the catalytic activity of ferromagnetic $CoFe_2O_4$ be enhanced [25]. Additionally, several reports have observed that the electrons/holes recombination of photocatalysts ($ZnFe_2O_4$, $Ti_{0.936}O_2$, Mn-$CsPbBr_3$) can be suppressed by magnetic field through manipulating their carrier transfer [22,24,27]. Inspired by these reports, it is expected that $BiVO_4$ photoanode coupling with amorphous magnetic co-catalysts under magnetic field may drive solar water oxidation more efficiently through weakening the carrier secondary recombination in/on co-catalysts.

At present, there are few investigations on the magnetic field impacting amorphous magnetic co-catalysts/photoanode systems. Herein, amorphous $Co_{0.07}Fe_{0.93}O_x$ nanoparticles with magnetic property were coupled on $BiVO_4$ films to form $BiVO_4/Co_{0.07}Fe_{0.93}O_x$ (BVO/CFO) films, which were further studied as photoanodes for solar water oxidation under magnetic field. In magnetic field-free condition, BVO/CFO film photoanode showed higher solar water oxidation activity than $BiVO_4$ (BVO) film photoanode, due to the presence of CFO co-catalysts. Under an external magnetic field of 8 mT, the solar water oxidation activity of BVO film photoanode was increased by 2.98% through magnetic field weakening the nonradiative recombination of carrier, relative to it in magnetic field-free condition. Interestingly, the activity of BVO/CFO film photoanode for solar water oxidation under same magnetic field was improved by 29.83%, which was 10 times to the improvment on BVO film photoanode. Integrated investigations revealed that magnetic field can significantly reduce the carrier secondary recombination in/on amorphous CFO co-catalysts to boost BVO/CFO film photoanode for water oxidation, but not change the water oxidation kinetics obviously. The present work provides insight into the effect of magnetic field on amorphous magnetic co-catalysts/photoanodes for solar water splitting, which could provide reference for the design of efficient photoelectrode systems.

2. Experimental section

2.1. Materials synthesis

2.1.1. Preparation of $BiVO_4$ films

$BiVO_4$ films were prepared on fluorine-doped tin oxide glass (FTO, 1 cm×2 cm, sheet resistance<15 Ω) by following procedures. First of all, a BiOI layer was prepared on FTO by an electrodeposition approach that is similar with our previous work [28]. Then, 80 μL of 0.2 M $VO(acac)_2$ (Aladdin) dimethyl sulfoxide solution was dripped on the as-prepared BiOI layer, and annealed in air at 450 °C for 120 min to form $BiVO_4$ film with excess V_2O_5. Finally, the excess V_2O_5 in/on $BiVO_4$ film was removed by soaking the film into 1 M NaOH for 30 min with gentle stirring. The electrodeposition of BiOI layer on FTO was conducted as follows. 50 mL of mixed aqueous solution containing 40 mM Bi $(NO_3)_3{\cdot}5H_2O$ (Aladdin) and 400 mM KI (Sigma-Aldrich) was prepared, and the pH of this solution was adjusted to ~1.7 using 1 M HNO_3. Then, 20 mL of 0.23 M *p*-benzoquinone ethanol solution was added into the Bi $(NO_3)_3$/KI aqueous solution under stirring for 20 min. The resultant mixed solution was used as electrolyte for BiOI electrodeposition. In a three-electrode cell (WE: a piece of FTO; CE: Pt wire electrode; RE: saturated Ag/AgCl electrode), the electrodeposition was carried on a CH Instruments 760E workstation. A potential of −0.1 V *vs.* Ag/AgCl was applied on the FTO working electrode for 2 min at room temperature, which was equivalent to a total charge of 0.11 C/cm^2.

2.1.2. Preparation of $BiVO_4/Co_{0.07}Fe_{0.93}O_x$ films

The $BiVO_4/Co_{0.07}Fe_{0.93}O_x$ films were firstly synthesized via a hydrothermal method, and then followed a thermal treating process. Briefly, a prefabricated $BiVO_4$ film was placed at the bottom of a 50 mL Teflon autoclave with the conductive side facing upward. 40 mL of aqueous precursor solution containing 1 mM $CoCl_2{\cdot}6H_2O$ (Aladdin, 99%), 2 mM $Fe(NO_3)_3$ (Aladdin, 99%) and 5 mM urea (Aladdin, 99%) was carefully added into the autoclave, maintaining an 80% filling ratio. The hydrothermal reaction was conducted at 180 °C for 12 h. Subsequently, the film was collected, thoroughly rinsed with deionized water, and dried at 60 °C in ambient air. Finally, the sample was annealed at 350 °C for 2 h in air to form $BiVO_4/Co_{0.07}Fe_{0.93}O_x$ film.

2.1.3. Preparation of $BiVO_4$/FeOOH and $BiVO_4$/CoPi films

For comparison, $BiVO_4$/FeOOH films were synthesized via a photo-deposition method according to a related report [14]. The deposition solution was prepared by dissolving 5 mM $FeSO_4{\cdot}7H_2O$ (Aladdin, 99%) and 100 mM K_2SO_4 (Aladdin, 99%) in 60 mL of deionized water, yielding a pH of ~5.3 without further adjustment. The photo-deposition was conducted in a three-electrode configuration (WE: $BiVO_4$ film; CE: Pt wire electrode; RE: saturated Ag/AgCl electrode). Firstly, a potential of 0.139 V *vs.* Ag/AgCl was applied on the $BiVO_4$ film electrode in dark until the dark current stabilized below 3 μA/cm^2. Then, the $BiVO_4$ film electrode was illuminated by a xenon lamp with simulated solar spectrum (Beijing China Education Au-light *Co. Ltd.*) through a back-side irradiation with a light intensity of 3 mW/cm^2. The deposition was proceeded for 150 s under continuous stirring, achieving a total charge of 8.3 mC/cm^2. After the deposition, the as-formed $BiVO_4$/FeOOH film was rinsed with deionized water to remove residual electrolyte.

CoPi layer was coupled on $BiVO_4$ film by a electrodeposition method [29,30]. The deposition electrolyte was prepared with 0.5 mM $Co(NO_3)_2$ in 0.1 M potassium phosphate buffer (0.1 M K_2HPO_4 and KH_2PO_4, pH 6.7). In a three-electrode cell (WE: $BiVO_4$ film; CE: Pt wire electrode; RE: saturated Ag/AgCl electrode), the electrodeposition was carried on a CH Instruments 760E workstation. A constant potential of 0.95 V *vs.* Ag/AgCl was applied on $BiVO_4$ film electrode for 70 s to form CoPi layer on $BiVO_4$ film. After the deposition, the as-prepared $BiVO_4$/CoPi film was rinsed with deionized water to remove residual electrolyte.

2.2. Material characterization

The morphology and elemental composition of $BiVO_4$ and $BiVO_4/Co_{0.07}Fe_{0.93}O_x$ films were checked using a scanning electron microscope (SEM, Hitachi SU8200) with EDS mapping function. The crystal phase of samples was detected by X-ray diffractometer (XRD, Rigaku SmartLab diffractometer). The $BiVO_4/Co_{0.07}Fe_{0.93}O_x$ film was precision-thinned by focused ion beam (FIB, Thermo Scientific Helios 5 CX) to conduct transmission electron microscope (TEM) characterization. The resultant sample was measured by TEM (Talos F200S) equipped with EDS function (SUPER X) for high-resolution imaging and elemental mapping analysis. X-ray photoelectron spectroscopy (XPS) investigations for samples were performed on a ThermoFisher Nexsa XPS system. After the dissolution of films into 2.0 M HNO_3, the metal element content of BVO/CFO films was detected using inductively coupled plasma mass spectrometry (ICP-MS, Agilent ICP-MS 7850). The magnetic hysteresis loops of BVO, BVO/CFO, BVO/FeOOH and BVO/CoPi films were measured using a vibrating sample magnetometer (VSM, Lake Shore 7400) in an applied magnetic field ranging from −4000 Oe to 4000 Oe under room temperature. Transient surface photovoltage spectrum of films were detected using surface photovoltage spectroscopy (Beijing China

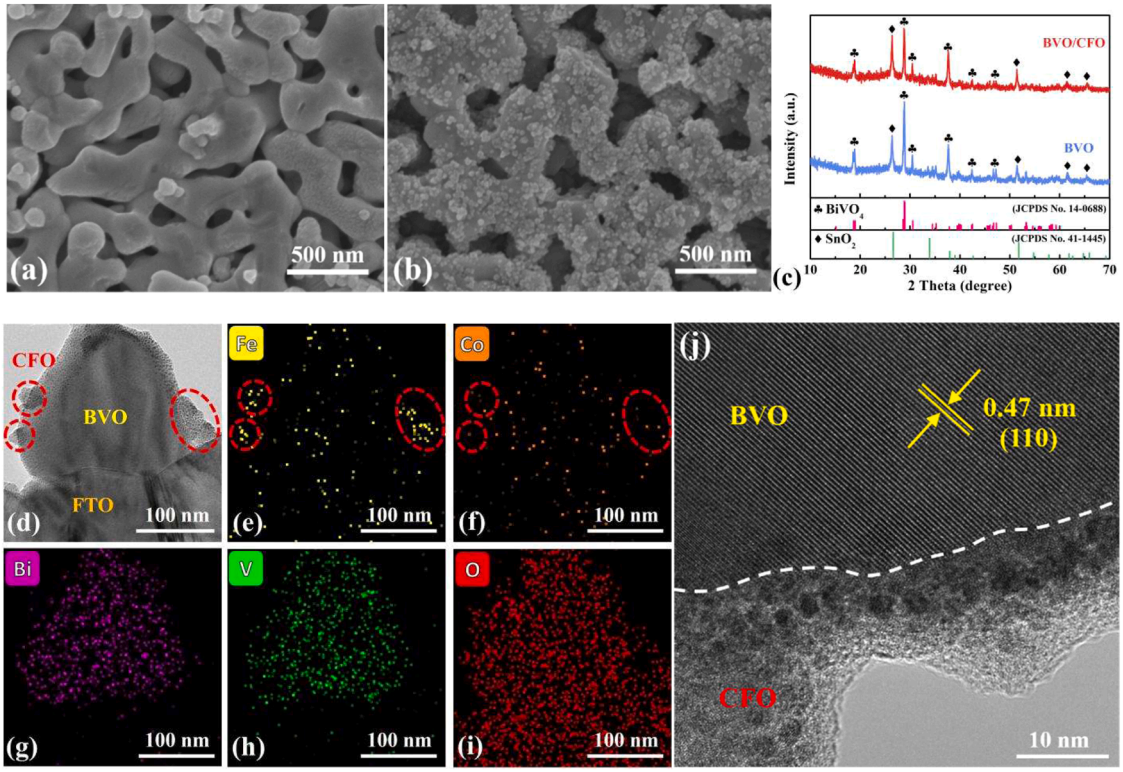

Fig. 1. Typical SEM images of (a) BVO and (b) BVO/CFO films. (c) XRD patterns of BVO and BVO/CFO films. (d) TEM image, (e–i) EDS mappings and (j) HRTEM image of BVO/CFO film.

Education Au-light *Co., Ltd.*, CEL-TPV2000). A piece of permanent magnet (1 cm×2 cm, ~8 mT) was stuck on the glass side of films to introduce magnetic field for measurement.

2.3. Photoelectrochemical measurements

The photoelectrochemical measurements were carried out on a CH Instruments 760E workstation with a three-electrode cell. The resultant film was the working electrode, a Pt wire electrode (99.99% of purity) and a saturated Ag/AgCl electrode (Shanghai Sanshe Instrument) were used as the counter electrode and reference electrode, respectively. 1.0 M borate buffer solution (KB, pH 9.3) was used as the electrolyte. For PEC measurements, a 300 W xenon lamp with an AM 1.5 G filter (Beijing China Education Au-light *Co. Ltd.*) provided 100 mW/cm^2 simulated sunlight irradiation. The PEC measurements were performed using back-side irradiation, in which the irradiation firstly passed through the FTO glass, and then reached on the film. During photoelectrochemical (PEC) measurements, an external MF (~8 mT at photoanode surface) was generated using a permanent magnet. Since magnet with strong magnetic field poses a safety risk during experimental operations, 8 mT magnetic field be selected to conduct experiments. The magnet was positioned parallel to the film photoanode and placed near to the electrochemical cell [8] (Fig. S1).

The testing potentials (*vs.* Ag/AgCl) were converted into the potentials *vs.* reversible hydrogen reference electrode (RHE) using Nernst equation.

$$E_{RHE} = E_{applied} + E_{ref} + 2.303 \times RT \times pH/F \quad (1)$$

where $E_{applied}$ is the applied potential, E_{ref} is the potential of Ag/AgCl reference electrode that be calibrated with respect to temperature, R is ideal gas constant (8.314 J·K^{-1}·mol^{-1}), T is the electrolyte temperature (K), pH is the pH value of electrolyte, and F is the Faraday constant (96,485 J·V^{-1}·mol^{-1}).

The applied bias photo-to-current efficiency (ABPE) of photoanodes was calculated using Eq. (2), assuming 100% Faradaic efficiency.

$$\text{ABPE}\ (\%) = j \times (1.23 - V_{bias})/P_{light} \times 100\% \quad (2)$$

where j is the photocurrent density (mA/cm^2) of photoanodes, V_{bias} is the potential on photoanode, and P_{light} represents the incident light power density (mW/cm^2).

According to the UV–Vis absorption spectrum, the light harvest efficiency (LHE) of $BiVO_4$ and $BiVO_4/Co_{0.07}Fe_{0.93}O_x$ films was determined by Eq. (3).

$$\text{LHE} = 1 - 10^{-\alpha(\lambda)} \quad (3)$$

where $\alpha(\lambda)$ is the absorbance at wavelength λ.

Assuming that the photon-current conversion efficiency of photoanodes was 100%, the photocurrent density corresponding to each wavelength was calculated by the following Eq. (4).

$$J_\lambda = J_{AM\ 1.5G} \times \text{LHE} \quad (4)$$

where $J_{AM\ 1.5\ G}$ is the standard photocurrent at each wavelength obtained from ASTM standard solar spectrum.

The charge separation efficiency ($\eta_{sep.}$) and charge injection efficiency ($\eta_{inj.}$) of film photoanodes were measured by Eq. (5 and 6).

$$\eta_{sep.} = j_{scavenger} \Big/ j_{abs} \quad (5)$$

$$\eta_{inj.} = j_{electrolyte} \Big/ j_{scavenger} \quad (6)$$

where j_{abs} is the integrated photocurrent density of film photoanode, $j_{electrolyte}$ is the photocurrent density of film photoanode in 1.0 M KB, and $j_{scavenger}$ is the photocurrent density of film photoanode in 1.0 M KB/0.2 M Na_2SO_3.

The electrochemical impedance spectroscopy (EIS) measurements for BVO/CFO film photoanode was carried out on a ModuLab XM ECS

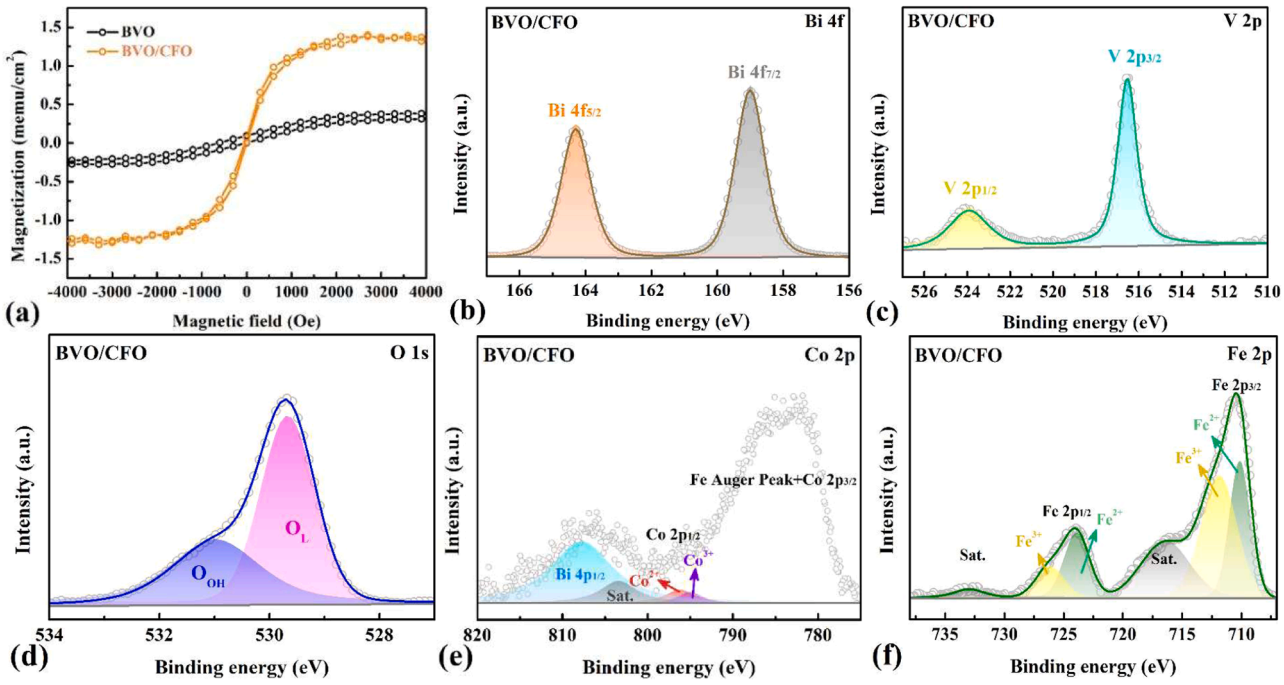

Fig. 2. (a) Hysteresis curves of BVO and BVO/CFO films. High-resolution XPS spectra of (b) Bi 4f, (c) V 2p, (d) O 1 s, (e) Co 2p and (f) Fe 2p of BVO/CFO film.

workstation and conducted in 1.0 M KB. The EIS measurements for BVO/CFO film photoanode were conducted at 0.6–0.8 V *vs.* RHE.The measurement frequency ranged from 0.1 to 100 000 Hz, and the amplitude was 5 mV. Based on the measured data, the EIS data was fitted using *ZView* software under equivalent circuit model.

Based on the Bode plots of BVO/CFO film photoanode, the lifetime of holes (τ_n) on photoanodes was calculated according to following equation.

$$\tau_n = 1 / 2\pi f_{max} \quad (7)$$

where f_{max} is the maximum frequency of the imaginary components.

3. Results and discussion

3.1. Characterization results

In the present work, CFO nanoparticles were coupled on BVO films to form BVO/CFO film photoanodes for solar water splitting. To optimize the preparation of BVO/CFO films, the PEC activity of the resultant BVO/CFO films was evaluated in 1.0 M KB under AM 1.5 G illumination with and without magnetic field (Fig. S1 in Supporting Information). According to the photocurrent observations, the BVO/CFO film that was annealed at 350 °C in air exhibited the highest activity (Figs. S2 and S3, Table S1). Consequently, this type BVO/CFO film was mainly investigated in subsequent sections. Fig. 1a shows the typical SEM image of BVO film, in which porous BVO being composed of irregular nanoparticles (200–400 nm) can be observed clearly. The morphology feature of BVO film is basically consistent with the reported $BiVO_4$ films that be prepared using similar electrodeposition and thermal treating approach [12]. After coupled with CFO, uniform CFO nanoparticles were appeared on BVO film (Fig. 1b). The presence of CFO nanoparticles on BVO film was further checked by EDS detection. As shown in Fig. S4, the EDS signals of Bi, V, O, Fe and Co elements were homogeneously detected. In addition, the content of Co, Fe, Bi and V of the BVO/CFO film was measured by ICP-MS. ICP-MS detections revealed that the Bi/V and Fe/Co atomic ratio of BVO/CFO film was close to 1.00/1.00 and 0.93/0.07, respectively (Table S2). Therefore, the stoichiometry of the as-synthesized CFO nanoparticles can be determined to be $Co_{0.07}Fe_{0.93}O_x$. Since $Co_{0.07}Fe_{0.93}O_x$ is formed by hydrothermal reaction in which Co/Fe ions may undergo different hydrolysis, precipitation, and deposition processes, the initial Co/Fe feeding ratio of 1:2 did not directly represent the final products of the Co/Fe oxide. In XRD detection, the diffraction peaks of monoclinic BVO (JCPDS No 14–0688) and FTO substrate (SnO_2, JCPDS No 41–1445) were observed (Fig. 1c) [31]. For BVO/CFO film, its XRD patterns were nearly identical to BVO film, suggesting that the CFO nanoparticles on BVO are amorphous. Combined focused ion beam treatment with TEM observation (Fig. S5), the BVO/CFO film was further investigated. In the TEM and HADDF-STEM images of BVO/CFO film, the presence of CFO nanoparticles on BVO surface can be observed (Figs. 1d and S6). The corresponding EDS mapping also indicated the uniform distribution CFO nanoparticles on BVO (Fig. 1e–i). Meanwhile, the amorphous CFO nanoparticles on monoclinic BVO surface was highlighted in the HRTEM image of BVO/CFO film (Fig. 1j). CFO nanoparticles had no lattice fringe, while BVO showed a lattice fringe of 0.47 nm that well matched to the (110) plane of monoclinic BVO [32,33]. Above characterization results suggested the successful coupling of amorphous CFO nanoparticles on BVO film to form BVO/CFO film.

The magnetic property of BVO and BVO/CFO films were compared at room temperature. As shown in Fig. 2a, BVO/CFO film shows higher magnetization than BVO film, indicating that the ferrimagnetic property of BVO/CFO film mainly stems from the presence of CFO nanoparticles on BVO film [22]. Furthermore, the chemical states of Bi, V, O, Co and Fe of BVO/CFO film were checked by XPS. In the XPS survey spectrum (Fig. S7), the characteristic signals of Bi, V, O, Co and Fe were detected, confirming the presence of BVO and CFO in BVO/CFO film. The typical Bi^{3+} and V^{5+} features of BVO were observed in the high-resolution spectra of Bi 4f and V 2p (Fig. 2b and c) [34]. In the high-resolution spectra of O 1 s (Fig. 2d), the peaks at 529.6 and 531.0 eV corresponded to the lattice oxygen and surface-adsorbed oxygen of BVO/CFO film, respectively [35]. In the high-resolution Co 2p spectra (Fig. 2e), the peaks located at 795.0 eV and 796.2 eV were assigned to Co^{3+} $2p_{1/2}$ and Co^{2+} $2p_{1/2}$, respectively [36,37]. In addition, the peaks corresponding to Co $2p_{3/2}$ (Co^{3+} ~780 eV, Co^{2+} ~783 eV) [36,37], Fe Auger peak (~786 eV) [38], and the Bi $4p_{1/2}$ peak of BVO (806.8 eV) [39] were observed in the 775–790 eV range of high-resolution Co 2p spectra. The

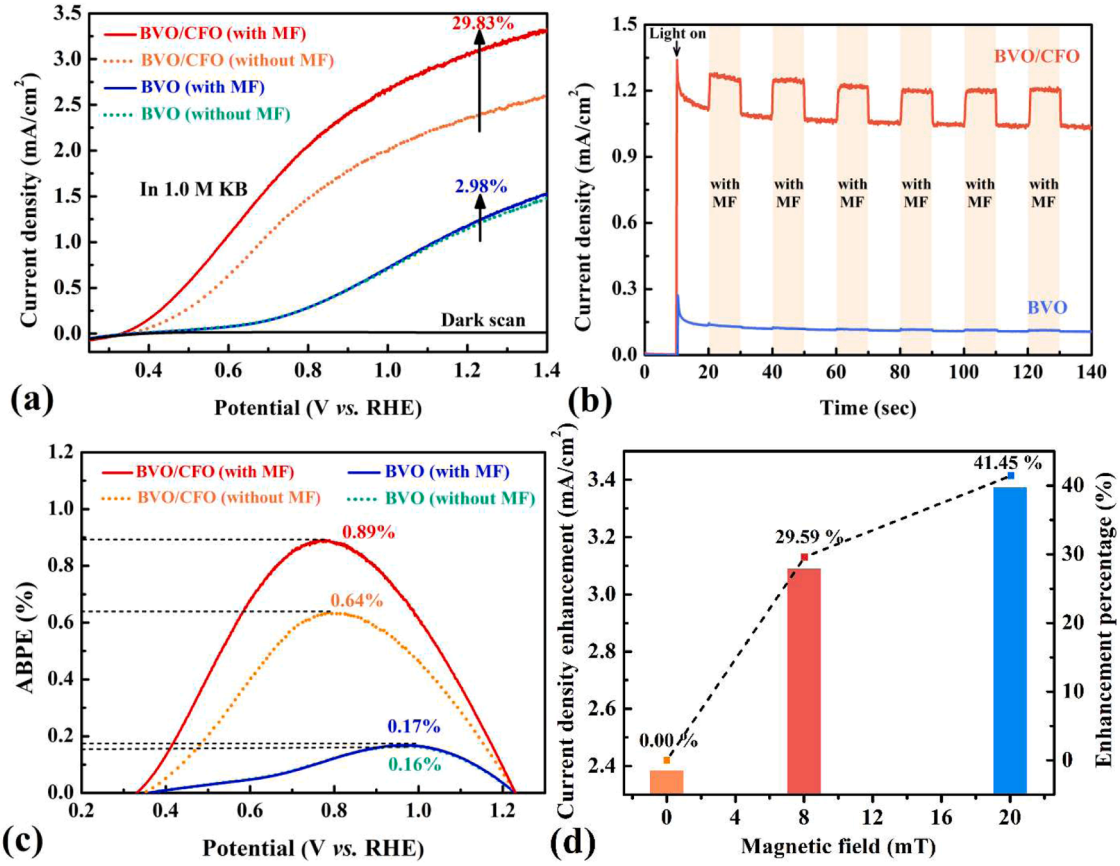

Fig. 3. (a) Under and without magnetic field, LSV curves for BVO and BVO/CFO film in 1.0 M KB under AM 1.5 G irradiation. (b) *j*-t curves of BVO and BVO/CFO film in 1.0 M KB at 0.7 V *vs.* RHE under AM 1.5 G irradiation with magnetic field in/off switching. (c) ABPE of BVO and BVO/CFO film photoanodes under and without magnetic field in 1.0 M KB. (d) Photocurrent change on BVO/CFO film with magnetic field intensity in 1.0 M KB under AM 1.5 G irradiation at 1.23 V *vs.* RHE.

high-resolution Fe 2p spectra exhibited the characteristic peaks of Fe^{2+} $2p_{3/2}$ (710.1 eV) and Fe^{2+} $2p_{1/2}$ (723.9 eV), along with the Fe^{3+} $2p_{3/2}$ (711.8 eV) and $Fe^{3+}2p_{1/2}$ (726.1 eV) (Fig. 2f) [40]. Based on the characterization findings, obvious solar water oxidation activity difference between BVO film and BVO/CFO film photoanodes in following activity investigations should be closely related to the presence of amorphous CFO magnetic nanoparticles on BVO film.

3.2. *The solar water oxidation performance of BVO/CFO film photoanode under magnetic field*

Fig. 3a displays the LSV curves for the BVO and BVO/CFO film under and without magnetic field in 1.0 M KB electrolyte under AM 1.5 G irradiation, respectively. In the absence of magnetic field, higher photocurrent density as well as lower photocurrent onset potential were observed on the BVO/CFO film compared to the BVO film. The onset potential of photocurrent on the BVO/CFO film was 0.32 V *vs.* RHE, while 0.50 V *vs.* RHE on the BVO film. At 1.23 V *vs.* RHE, the photocurrent density of the BVO/CFO film was 2.380 mA/cm^2, which is more than double that of the BVO film (1.205 mA/cm^2). In previous reports, the photocurrent on BVO-based films in KB electrolyte under AM 1.5 G irradiation has been demonstrated to be mainly produced from solar water oxidation reaction [12,14,17]. In dark condition, lower onset potential and Tafel slope of oxygen evolution reaction were found on the BVO/CFO film electrode than the BVO film electrode in 1.0 M KB electrolyte, suggesting the co-catalysis of CFO for water oxidation [41]

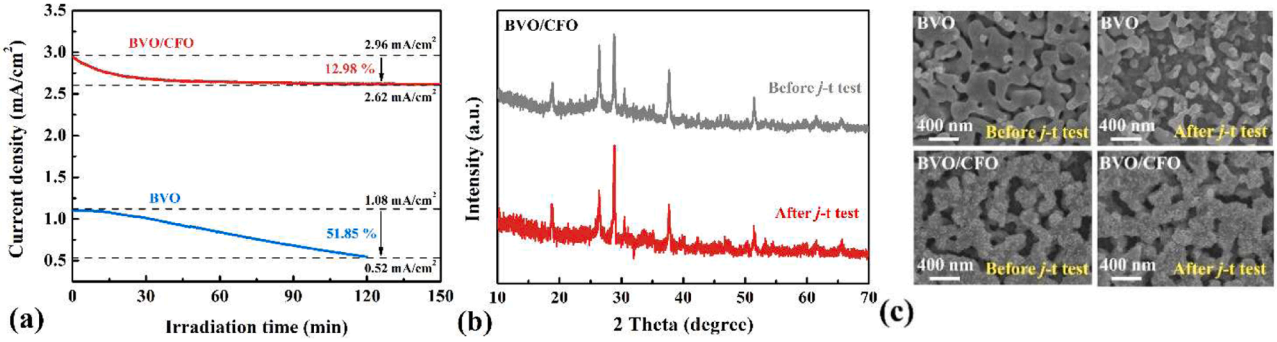

Fig. 4. (a) *j*-t curves of BVO and BVO/CFO photoanodes at 1.23 V *vs.* RHE under magnet filed. (b) Comparative XRD patterns of BVO/CFO film photoanode before and after stability testing. (c) Comparative SEM images of BVO and BVO/CFO film photoanode before and after stability testing.

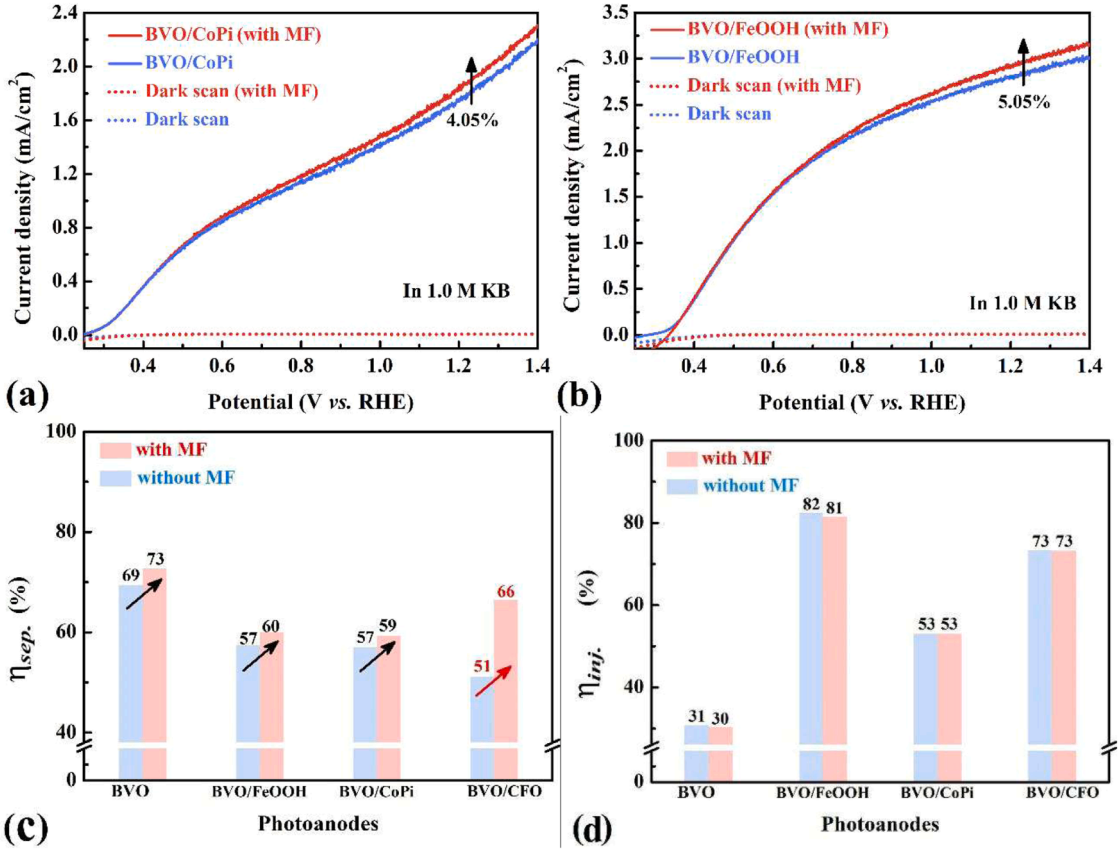

Fig. 5. Under and without magnetic field, LSV curves for (a) BVO/CoPi and (b) BVO/FeOOH film in 1.0 M KB under AM 1.5 G irradiation. (c) $\eta_{sep.}$ and (d) $\eta_{inj.}$ of BVO, BVO/CoPi, BVO/FeOOH and BVO/CFO film photoanodes in 1.0 M KB at 1.23 V *vs.* RHE.

(Fig. S8). These outcomes indicated that BVO/CFO film can work as better photoanode for solar water oxidation than BVO film, due to the presence of CFO co-catalysts on BVO film. After the introduction of a magnetic field of ~8 mT on film surface, the water oxidation photocurrent on the BVO/CFO film was obviously enhanced but the photocurrent onset potential was basically unchanged. Specifically, the photocurrent density on the BVO/CFO film under magnetic field at 1.23 V *vs.* RHE was improved from 2.380 mA/cm^2 to 3.090 mA/cm^2, achieving 29.8% improvment. For three more independent BVO/CFO films, the photocurrent enhancement under magnetic field was repeatably observed (Fig. S9). For the BVO film, its photocurrent under magnetic field was also increased (at 1.23 V *vs.* RHE, 1.205 mA/cm^2 to 1.241 mA/cm^2, 2.98% improvment), but not significant as the BVO/CFO film. The photocurrent increase difference between BVO and BVO/CFO film under magnetic field can be further observed at 0.7 V *vs.* RHE (Fig. 3b) and ECSA-normalized condition (Fig. S10 and Table S3). Similar finding was observed in their ABPE, OCP change and transient photocurrent response detections in the absence and presence of magnetic field, in which the BVO/CFO film exhibited higher ABPE increase and OCP change than the BVO film (Fig. 3c and S11) [42–44]. The influance of magnetic field intensity on the water oxidation photocurrent and ABPE of BVO/CFO film was shown in Fig. S12 and 3d In general, the photocurrent and ABPE of BVO/CFO film were improved with the increase of magnetic field intensity, further confirming the positive impact of magnetic field on the solar water oxidation activity of BVO/CFO film photoanode.

The water oxidation photocurrent on BVO and BVO/CFO film photoanode under magnetic field at 1.23 V *vs.* RHE was shown in Fig. 4a. Obviously, the BVO/CFO film photoanode had more stable activity for water oxidation than the BVO film photoanode under magnetic field. After 150 min testing, the water oxidation photocurrent of the BVO/CFO film photoanode was generally kept at 2.62 mA cm^{-2}, and its activity decay rate was 12.98%. For the BVO film photoanode, only 0.52 mA cm^{-2} water oxidation photocurrent was maintained after 120 min testing, namely 51.85% activity remaining. Comparative XRD detection and SEM observation indicated that the BVO/CFO film photoanode has slight change in crystal phase and morphology after 150 min testing (Fig. 4b and c). By comparison, obvious morphology change was observed on the BVO film photoanode after 120 min testing, due to the presence of surface micro-dissolution caused by photocorrosion. The stability testing and comparative characterization results suggested the promoting effect of CFO co-catalysts and magnetic field on the water oxidation durability of BVO film photoanode.

3.3. *The mechanism of BVO/CFO film photoanode with enhanced solar water oxidation performance under magnetic field*

It is noteworthy that the UV–Vis absorption feature of BVO and BVO/CFO film is very similar (Fig. S13). This observation suggested that their photocurrent difference is not mainly caused by their difference in light harvesting property. Above hysteresis results indicated that the presence of amorphous CFO nanoparticles on BVO film induces the obvious magnetic response of BVO/CFO film (Fig. 2a). Under magnetic field, the more significant activity improvement on BVO/CFO film photoanode than BVO film photoanode should be closely related to the magnetic property of amorphous CFO co-catalysts. To understand the relevance of amorphous co-catalysts' magnetic property to the activity of BVO/co-catalysts photoanodes under magnetic field, the solar water oxidation activity changes of BVO/CoPi and BVO/FeOOH film was measured under and without magnetic field. As shown in Fig. 5a and b, the water oxidation photocurrent on BVO/CoPi and BVO/FeOOH film under magnetic field was improved to some extent. Relative to without

Table 1
Under and without magnetic field, the photocurrent increase on BVO, BVO/CoPi, BVO/FeOOH and BVO/CFO film in 1.0 M KB at 1.23 V *vs.* RHE.

Sample	Photocurrent without MF	Photocurrent in MF	Increase percentage
BVO	2.01 mA/cm^2	2.15 mA/cm^2	2.98%
BVO/CoPi	2.21 mA/cm^2	2.69 mA/cm^2	4.05%
BVO/FeOOH	2.38 mA/cm^2	3.09 mA/cm^2	5.01%
BVO/CFO	2.38 mA/cm^2	3.09 mA/cm^2	29.83%

magnetic field, the photocurrent increase on BVO/CoPi and BVO/FeOOH film at 1.23 V *vs.* RHE under magnetic field was 4.05% and 5.01%, respectively, which is close to the BVO film (2.56%) but much lower than that of BVO/CFO film (29.83%) (Table 1). In addition, the $\eta_{sep.}$ and $\eta_{inj.}$ of BVO, BVO/FeOOH, BVO/CoPi and BVO/CFO film photoanodes under and without magnetic field were measured and compared. As displayed in Figs. 5c, S14–S16, the BVO film photoanode has the highest $\eta_{sep.}$ among four different photoanodes in magnetic field-free condition, since amorphous co-catalysts usually lack selectivity for the extraction of holes/electrons from BVO and thereby result in carrier secondary recombination in/on co-catalysts [12]. The transient current features of BVO and BVO/CFO film under AM1.5 G on/off conditions also suggested that amorphous CFO co-catalysts coupling on BVO film does not preferentially transfer either photogenerated electrons or holes from BVO film (Fig. S17). Under magnetic field, the $\eta_{sep.}$ of BVO, BVO/FeOOH and BVO/CoPi film photoanodes was only increased 2% ~4% (Figs. 5c and S15), due to magnetic field suppressing the non-radiative recombination of carrier [8]. But for the BVO/CFO film photoanode, its $\eta_{sep.}$ was significantly increased from 51% to 66% under magnetic field, suggesting that the as-extracted holes/electrons in/on CFO co-catalysts from BVO film be effectively separated under magnetic field. By comparison, magnetic field nearly has no effect on the $\eta_{inj.}$ of BVO, BVO/FeOOH, BVO/CoPi and BVO/CFO film photoanodes (Figs. 5d and S15). Hysteresis measurements indicated that amorphous CoPi and FeOOH co-catalysts have no magnetic property (Fig. S18). Fundamentally, the η_{sep} of photoanodes reflects the carrier separation feature in/on photoanodes, while $\eta_{inj.}$ displays the injecting feature of carrier in/on photoanodes reacting with H_2O molecules. From the $\eta_{sep.}$ and $\eta_{inj.}$ changes on BVO/CFO film photoanode under and without magnetic field, it can be known that magnetic field has significant effect on weakening the carrier recombination in/on magnetic CFO co-catalysts, in addition to suppressing the nonradiative recombination of carrier in BVO film.

To know the solar water oxidation kinetics on BVO/CFO film photoanode under and without magnetic field, its EIS signals at different potentials were comparatively recorded. As exhibited in Fig. 6a–e, smaller arc can be observed in the Nyquist plots of BVO/CFO film photoanode under magnetic field, relative to it in magnetic field-free condition. EIS Fitting indicated that the reaction resistance (R_{ct}) of BVO/CFO film photoanode during water oxidation under magnetic field is lower than that in magnetic field-free condition (Table S4, Fig. 6f). For PEC water oxidation, if the holes on photoanodes can react with water molecules fast, short-lifetime holes will be detected on photoanodes. Significantly, the holes' lifetime (τ_n) on BVO/CFO film photoanode under magnetic field was found to be close to that in magnetic field-free condition (Figs. S19 and 6f), suggesting similar kinetics of holes reacting with H_2O molecules. In addition, the onset potential and Tafel slope of water oxidation on BVO/CFO film electrode under and without magnetic field not be changed obviously (Fig. S20). In principle, R_{ct} is a general reflection for the water oxidation kinetics of photoanodes, which involves charge transfer resistance and water oxidation resistance. From above results, it can be deduced that magnetic field cannot boost the water oxidation kinetics of BVO/CFO film photoanode. It has been reported that magnetic Fe-based and Co-based oxides under magnetic field have negative magnetoresistance effect, namely magnetic field can improve the carrier transfer in/on magnetic Fe-based and Co-based oxides [22,24,27]. Therefore, the enhanced activity on BVO/CFO film photoanode under magnetic field mainly originates from magnetic field improving carrier transfer in/on magnetic CFO co-catasts, namely reducing the carrier secondary recombination in/on magnetic CFO co-catasts.

To further understand the origin of higher water splitting activity on BVO/CFO film photoanode under magnetic field, its transient surface photovoltage (TSPV) was measured under and without magnetic field. As depicted in Fig. 7a, the surface photovoltage of BVO/CFO film under

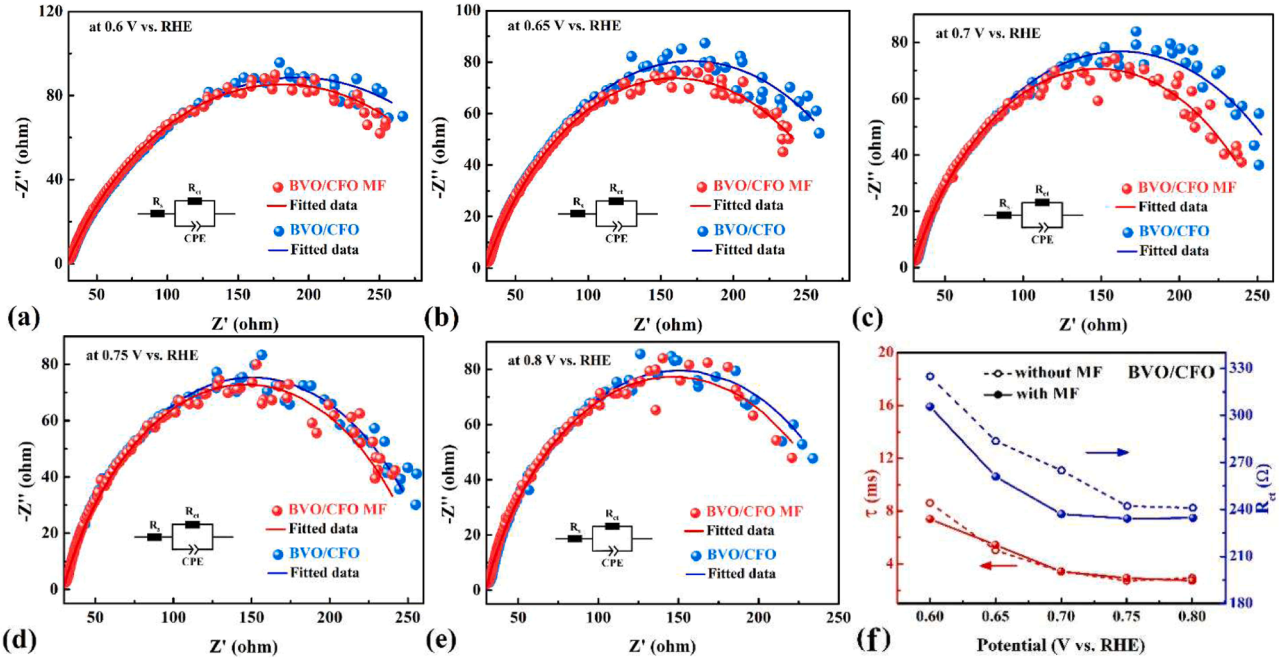

Fig. 6. Under and without magnetic field, Nyquist plots of BVO/CFO film photoanode at (a) 0.6 V, (b) 0.65 V, (c) 0.7 V, (d) 0.75 V and (e) 0.8 V *vs.* RHE in 1.0 M KB (Inset: fitted equivalent circuit), (f) R_{ct} and τ_n of BVO/CFO film photoanodes at 0.60~0.80 V *vs.* RHE.

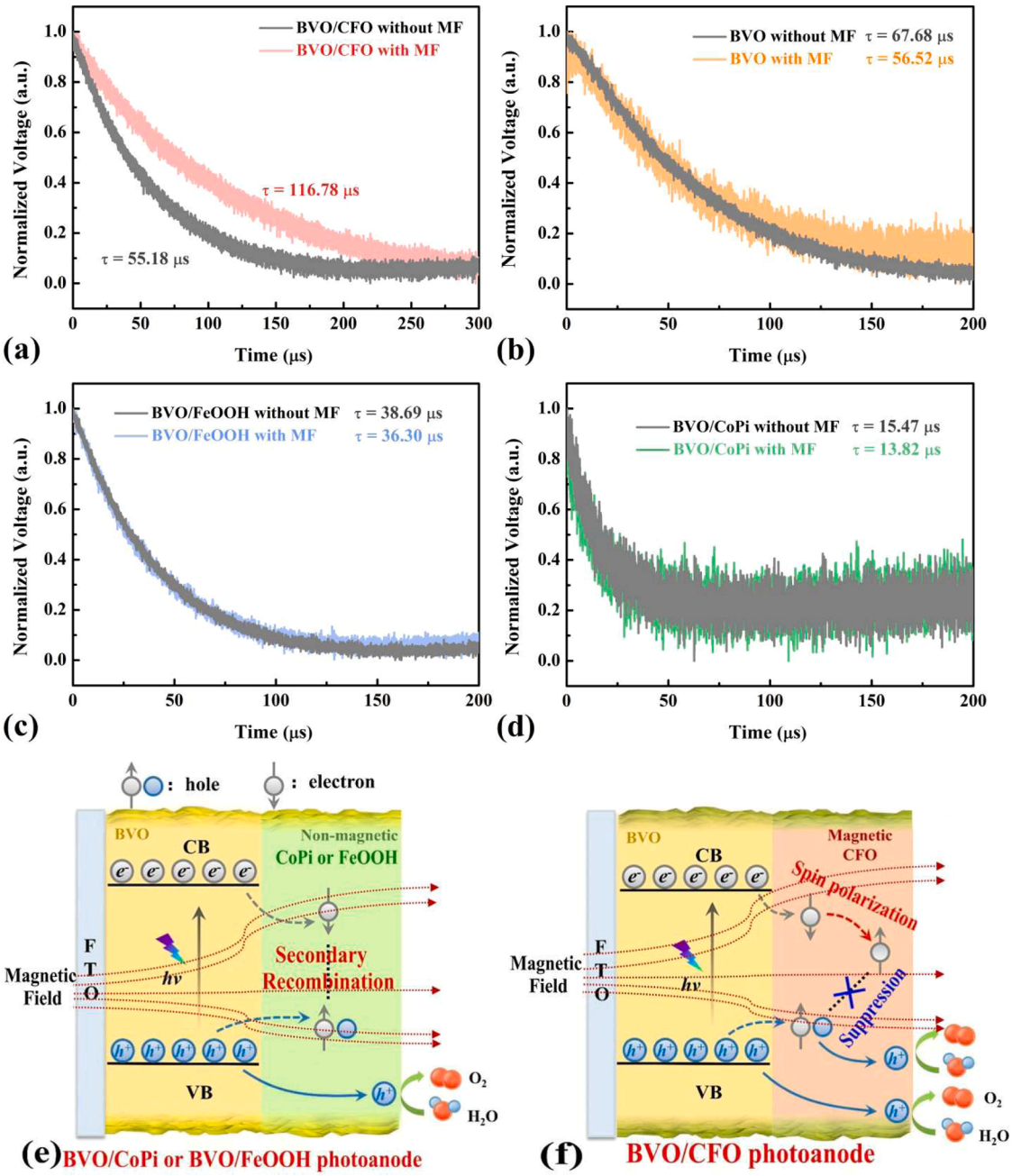

Fig. 7. TSPV results of (a) BVO/CFO, (b) BVO, (c) BVO/FeOOH and (d) BVO/CoPi films under and without magnetic field. (e) Diagram of (e) BVO/FeOOH or BVO/CoPi film, and (f) BVO/CFO photoanode under magnetic field for solar water splitting.

magnetic field is higher than that in magnetic field-free condition. Further analysis revealed that the carrier lifetime of BVO/CFO film under magnetic field is ~116.78 μs), which is markedly longer than that in magnetic field-free condition (~55.18 μs). In the TSPV observations for BVO, BVO/FeOOH and BVO/CoPi films, their surface photovoltage under magnetic field was higher than in magnetic field-free condition, but not obvious as the variation range on BVO/CFO film (Fig. 7b–d). Furthermore, the carrier lifetimes of BVO, BVO/FeOOH and BVO/CoPi films exhibited slightly longer under magnetic field than without magnetic field, indicating that magnetic field has not significant influence on the carrier recombination in/on non-magnetic systems (BVO, BVO/FeOOH and BVO/CoPi films). According to the Pauli exclusion principle, carrier recombination in/on semiconductors requires spin-matching configuration, *i.e.* electron/hole pairs within the same orbital needs to have opposite spin-orientation. In magnetic materials, the unpaired electrons will easily be spin-polarized in magnetic field [22,24,27], which reduces the population of spin-opposite electron-hole pairs available for recombination. Since spin-flip processes demand additional energy, the time required for spin-matching in magnetic materials is significantly prolonged, thereby extending carrier lifetimes. It should be noted that the applied magnetic field in the present work was relatively low (mT level) that is insufficient to induce noticeable convection in aqueous electrolytes and change mass transport obviously.

On the basis of above results, the carrier recombination in/on BVO/amorphous non-magnetic co-catalysts photoanodes and BVO/amorphous magnetic co-catalysts photoanodes can be presented as the diagrams shown in Fig. 7e and f, respectively. Due to the presence of amorphous co-catalysts on BVO film, its carrier can be transferred from BVO to co-catalysts through contact interfaces. When the electrons and holes reached the amorphous co-catalysts, they may trigger carrier

secondary recombination in/on amorphous co-catalysts. With the introduction of magnetic field, magnetic field has weak suppressing effect on the nonradiative recombination of carrier in BVO film, but no obvious impact on the carrier secondary recombination in/on amorphous non-magnetic co-catalysts (such as, CoPi, FeOOH) (Fig. 7e). For BVO/CFO film, magnetic field could induce the spin polarization of amorphous magnetic CFO, and reduce the carrier secondary recombination in/on CFO co-catasts. As a result, BVO/CFO film as photoanode under magnetic field has higher activity for solar water oxidation (Fig. 7f).

4. Conclusion

In summary, amorphous CFO nanoparticles with magnetic property were coupled on $BiVO_4$ film to form BVO/CFO film photoanode for solar water oxidation under magnetic field. In magnetic field-free condition, the BVO/CFO film photoanode had higher solar water oxidation activity (2.380 mA/cm^2 at 1.23 V *vs.* RHE) than BVO film photoanode (1.205 mA/cm^2 at 1.23 V *vs.* RHE), due to the presence of CFO co-catalysis. Under an external magnetic field of 8 mT at 1.23 V *vs.* RHE, the solar water oxidation activity of BVO film photoanode was increased by 2.98% through magnetic field weakening the nonradiative recombination of carrier, relative to it in magnetic field-free condition. For BVO/CFO film photoanode, its activity for solar water oxidation under same magnetic field was improved by 29.83% (2.38 mA/cm^2 to 3.09 mA/cm^{2}at 1.23 V *vs.* RHE). In addition, the BVO/CFO film photoanode showed more stable activity during continuous water oxidation than BVO film photoanode under magnetic field. Mechanism investigations revealed that magnetic field can significantly reduce the carrier secondary recombination in/on amorphous magnetic CFO co-catalysts to boost BVO/CFO film photoanode for solar water oxidation, but not change the reaction kinetics obviously. The present work provides insight into the effect of magnetic field on amorphous co-catalysts/photoanodes for solar water splitting, which could reference for the design of efficient photoelectrodes system.

CRediT authorship contribution statement

Yujie Huang: Methodology, Investigation, Data curation. **Jinyan Du:** Investigation, Formal analysis, Data curation. **Xianchun Jin:** Resources, Methodology. **Jiahe Li:** Formal analysis, Data curation. **Lingling Liao:** Data curation. **Tao Han:** Resources. **Gaili Ke:** Writing – review & editing, Resources, Conceptualization. **Huichao He:** Supervision, Resources, Funding acquisition.

Declaration of competing interest

The authors declare that they have no known competing financial interests or personal relationships that could have appeared to influence the work reported in this paper.

Acknowledgments

This work was supported by Natural Science Foundation of Chongqing (CSTB2025NSCQ-WZQLHJJMSX0011), Research Foundation of Chongqing University of Science and Technology (no ckrc2022003).

Supplementary materials

Supplementary material associated with this article can be found, in the online version, at doi:10.1016/j.electacta.2026.149211.

Data availability

Data will be made available on request.

References

[1] S.Y. Reece, J.A. Hamel, K. Sung, T.D. Jarvi, A.J. Esswein, J.J. Pijpers, D.G. Nocera, Wireless solar water splitting using silicon-based semiconductors and earth-abundant catalysts, Science 334 (2011) 645–648.
[2] H. Nishiyama, T. Yamada, M. Nakabayashi, Y. Maehara, M. Yamaguchi, Y. Kuromiya, Y. Nagatsuma, H. Tokudome, S. Akiyama, T. Watanabe, Photocatalytic solar hydrogen production from water on a 100-m^2 scale, Nature 598 (2021) 304–307.
[3] P. Zhou, I.A. Navid, Y. Ma, Y. Xiao, P. Wang, Z. Ye, B. Zhou, K. Sun, Z. Mi, Solar-to-hydrogen efficiency of more than 9% in photocatalytic water splitting, Nature 613 (2023) 66–70.
[4] V. Andrei, B. Reuillard, E. Reisner, Bias-free solar syngas production by integrating a molecular cobalt catalyst with perovskite $BiVO_4$ tandems, Nat. Mater. 19 (2020) 189–194.
[5] V. Andrei, R.A. Jagt, M. Rahaman, L. Lari, V.K. Lazarov, J.L. MacManus-Driscoll, R. L. Hoye, E. Reisner, Long-term solar water and CO_2 splitting with photoelectrochemical BiOI/$BiVO_4$ tandems, Nat. Mater. 21 (2022) 864–868.
[6] V. Andrei, G.M. Ucoski, C. Pornrungroj, C. Uswachoke, Q. Wang, D.S. Achilleos, H. Kasap, K.P. Sokol, R.A. Jagt, H. Lu, Floating perovskite-$BiVO_4$ devices for scalable solar fuel production, Nature 608 (2022) 518–522.
[7] C. Zhen, X. Chen, R. Chen, F. Fan, X. Xu, Y. Kang, J. Guo, L. Wang, G.Q. Lu, K. Domen, Liquid metal-embraced photoactive films for artificial photosynthesis, Nat. Commun. 15 (2024) 1672.
[8] Q. Yang, J. Du, X. Nie, D. Yang, L. Bian, L. Yang, F. Dong, H. He, Y. Zhou, H. Yang, Magnetic field-assisted photoelectrochemical water splitting: the photoelectrodes have weaker nonradiative recombination of carrier, ACS Catal. 11 (2021) 1242–1247.
[9] R.T. Gao, D. He, L. Wu, K. Hu, X. Liu, Y. Su, L. Wang, Towards long term photostability of nickel hydroxide/$BiVO_4$ photoanodes for oxygen evolution catalysts via *in situ* catalyst tuning, Angewand. Chem. 132 (2020) 6272–6277.
[10] B. Liu, X. Wang, Y. Zhang, L. Xu, T. Wang, X. Xiao, S. Wang, L. Wang, W. Huang, A $BiVO_4$ photoanode with a VO_x layer bearing oxygen vacancies offers improved charge transfer and oxygen evolution kinetics in photoelectrochemical water splitting, Angewand. Chem. 135 (2023) e202217346.
[11] J. Wang, J. Sun, Y. Liu, X. Zhang, K. Cheng, Y. Chen, F. Zhou, J. Luo, T. Li, J. Guo, The CuSCN layer between $BiVO_4$ and $NiFeO_x$ for facilitating photogenerated carrier transfer and water oxidation kinetics, J. Colloid Interface Sci. 666 (2024) 57–65.
[12] T.W. Kim, K.-S. Choi, Nanoporous $BiVO_4$ photoanodes with dual-layer oxygen evolution catalysts for solar water splitting, Science 343 (2014) 990–994.
[13] Y. Kuang, Q. Jia, G. Ma, T. Hisatomi, T. Minegishi, H. Nishiyama, M. Nakabayashi, N. Shibata, T. Yamada, A. Kudo, Ultrastable low-bias water splitting photoanodes via photocorrosion inhibition and *in situ* catalyst regeneration, Nat. Energy 2 (2016) 1–9.
[14] D.K. Lee, K.-S. Choi, Enhancing long-term photostability of $BiVO_4$ photoanodes for solar water splitting by tuning electrolyte composition, Nat. Energy 3 (2018) 53–60.
[15] C. Li, M. Chen, Y. Xie, H. Wang, L. Jia, Boosting photoelectrochemical water splitting of bismuth vanadate photoanode via novel co-catalysts of amorphous manganese oxide with variable valence states, J. Colloid Interface Sci. 636 (2023) 103–112.
[16] X. Lu, K.-h. Ye, S. Zhang, J. Zhang, J. Yang, Y. Huang, H. Ji, Amorphous type FeOOH modified defective $BiVO_4$ photoanodes for photoelectrochemical water oxidation, Chem. Eng. J. 428 (2022) 131027.
[17] S. Wang, P. Chen, Y. Bai, J.H. Yun, G. Liu, L. Wang, New $BiVO_4$ dual photoanodes with enriched oxygen vacancies for efficient solar driven water splitting, Adv. Mater. 30 (2018) 1800486.
[18] D. Tang, J. Liu, Y. Pang, L. Wu, F. Xu, M. Cen, H. Yang, M.-S. Balogun, J. Chen, Y.-w. Hu, Amorphous topological buffer layer engineering enables ultralong cycling stability trifunctional electrocatalysis for integrated energy systems, Chem. Eng. J. 526 (2025) 170876.
[19] X. Chen, X. Li, Y. Peng, H. Yang, Y. Tong, M.S. Balogun, Y. Huang, Tailoring carrier dynamics of $BiVO_4$ photoanode via dual incorporation of Au and $Co(OH)_x$ cooperative modification for photoelectrochemical water splitting, Adv. Funct. Mater. 35 (2025) 2416091.
[20] Y. Pang, L. Wu, J. Liu, D. Tang, F. Xu, M. Cen, Z. Wang, Y. Xie, H. Yang, M. S. Balogun, Tunable surface charge redistribution via lattice strain engineering in B/MoCo-doped NiV_2O_6 for high power supercapacitors, Adv. Funct. Mater. 35 (2025) 2506747.
[21] X.-D. Dong, Z.-Y. Zhao, Boosting and regulating solar energy conversion performance of delafossite $AgFeO_2$ by spin polarization, J. Mater. Chem. A 10 (2022) 4800–4816.
[22] W. Gao, R. Peng, Y. Yang, X. Zhao, C. Cui, X. Su, W. Qin, Y. Dai, Y. Ma, H. Liu, Electron spin polarization-enhanced photoinduced charge separation in ferromagnetic $ZnFe_2O_4$, ACS Energy Lett. 6 (2021) 2129–2137.
[23] G. Li, X. Sun, P. Chen, M. Song, T. Zhao, F. Liu, S.-F. Yin, Insights into spin polarization regulated exciton dissociation and charge separation of C_3N_4 for efficient hydrogen evolution and simultaneous benzylamine oxidation, Nano Res. 16 (2023) 8845–8852.
[24] L. Pan, M. Ai, C. Huang, L. Yin, X. Liu, R. Zhang, S. Wang, Z. Jiang, X. Zhang, J.-J. Zou, Manipulating spin polarization of titanium dioxide for efficient photocatalysis, Nat. Commun. 11 (2020) 418.
[25] X. Ren, T. Wu, Y. Sun, Y. Li, G. Xian, X. Liu, C. Shen, J. Gracia, H.-J. Gao, H. Yang, Spin-polarized oxygen evolution reaction under magnetic field, Nat. Commun. 12 (2021) 2608.

[26] Y.-l. Wang, T.-h. Yang, S. Yue, H.-b. Zheng, X.-p. Liu, P.-z. Gao, H. Qin, H.-n. Xiao, Effects of alternating magnetic fields on the OER of heterogeneous core-shell structured $NiFe_2O_4$@(Ni, Fe)S/P, ACS Appl. Mater. Interface. 15 (2023) 11631–11641.
[27] C.-C. Lin, T.-R. Liu, S.-R. Lin, K.M. Boopathi, C.-H. Chiang, W.-Y. Tzeng, W.-H. C. Chien, H.-S. Hsu, C.-W. Luo, H.-Y. Tsai, Spin-polarized photocatalytic CO_2 reduction of Mn-doped perovskite nanoplates, J. Am. Chem. Soc. 144 (2022) 15718–15726.
[28] Y. Huang, B. Liu, Y. Yang, H. Xiao, T. Han, H. Jiang, J. Li, Y. Zhou, G. Ke, H. He, $BiVO_4$ film coupling with $CoAl_2O_4$ nanoparticles for photoelectrochemical water splitting utilizing broad solar spectrum through p-n heterojunction, photothermal, and cocatalytic synergism, Langmuir 40 (2024) 18670–18682.
[29] W. Fang, A. Qin, Y. Lin, R. Xv, L. Fu, A highly enhanced photoelectrochemical performance of $BiVO_4$ photoanodes modified with CoPi groups by increasing energy band bending, accelerating hole separation and improving water oxidation kinetics, Sustain. Energy Fuel. 6 (2022) 1075–1083.
[30] Y. Ma, A. Kafizas, S.R. Pendlebury, F. Le Formal, J.R. Durrant, Photoinduced absorption spectroscopy of CoPi on $BiVO_4$: the function of CoPi during water oxidation, Adv. Funct. Mater. 26 (2016) 4951–4960.
[31] Z. Xie, D. Chen, J. Zhai, Y. Huang, H. Ji, Charge separation via synergy of homojunction and electrocatalyst in $BiVO_4$ for photoelectrochemical water splitting, Appl. Cataly. B: Environ. 334 (2023) 122865.
[32] H. Chu, S. Zheng, Y. Li, K. Xu, Q. Hong, T. Li, W. Ren, S. Li, Z. Mei, F. Pan, Tuning the exposure of $BiVO_4$-{010} facets to enhance the N_2 photofixation performance, RSC Adv. 11 (2021) 28908–28911.
[33] F. Feng, D. Mitoraj, R. Gong, D. Gao, M.M. Elnagar, R. Liu, R. Beranek, C. Streb, High-performance $BiVO_4$ photoanodes: elucidating the combined effects of Mo-doping and modification with cobalt polyoxometalate, Materials Advances 5 (2024) 4932–4944.
[34] Y. Lu, Y. Yang, X. Fan, Y. Li, D. Zhou, B. Cai, L. Wang, K. Fan, K. Zhang, Boosting charge transport in $BiVO_4$ photoanode for solar water oxidation, Adv. Mater. 34 (2022) 2108178.
[35] S. Wang, P. Chen, J.H. Yun, Y. Hu, L. Wang, An electrochemically treated $BiVO_4$ photoanode for efficient photoelectrochemical water splitting, Angewand. Chem. Int. Edit. 56 (2017) 8500–8504.
[36] S. Liu, S.C. Lee, U. Patil, I. Shackery, S. Kang, K. Zhang, J.H. Park, K.Y. Chung, S. C. Jun, Hierarchical MnCo-layered double hydroxides@$Ni(OH)_2$ core-shell heterostructures as advanced electrodes for supercapacitors, J. Mater. Chem. A 5 (2017) 1043–1049.
[37] L. Dahron, R.m. Dedryvre, H. Martinez, M. Mntrier, C. Denage, C. Delmas, D. Gonbeau, Electron transfer mechanisms upon lithium deintercalation from $LiCoO_2$ to CoO_2 investigated by XPS, Chem. Mater. 20 (2008) 583–590.
[38] B. Han, E. Zhang, G. Cheng, Facile preparation of graphene oxide-MIL-101 (Fe) composite for the efficient capture of uranium, Appl. Sci. 8 (2018) 2270.
[39] A. Petala, A. Noe, Z. Frontistis, C. Drivas, S. Kennou, D. Mantzavinos, D. I. Kondarides, Synthesis and characterization of CoO_x/$BiVO_4$ photocatalysts for the degradation of propyl paraben, J. Hazard. Mater. 372 (2019) 52–60.
[40] C. Xia, Y. Li, M. Je, J. Kim, S.M. Cho, C.H. Choi, H. Choi, T.-H. Kim, J.K. Kim, Nanocrystalline iron pyrophosphate-regulated amorphous phosphate overlayer for enhancing solar water oxidation, Nano-Micro Lett. 14 (2022) 209.
[41] X. Cui, M. Wu, X. Liu, B. He, Y. Zhu, Y. Jiang, Y. Yang, Engineering organic polymers as emerging sustainable materials for powerful electrocatalysts, Chem. Soc. Rev. 53 (2024) 1447–1494.
[42] L. Shuai, Q. Li, J. Liu, J. Wu, X. Huang, J. Yu, J. Dou, H. Li, X. Chen, Rational design of $BiVO_4$/CoFe-LDH@$Ni_2(NO_3)_2(OH)_2$ ternary photoanodes: synergistic built-in electric field and oxygen vacancies for high-efficiency solar water oxidation, Int. J. Hydrog. Energy 177 (2025) 151556.
[43] L. Shuai, L. Tian, X. Huang, J. Yu, J. Dou, X. Chen, Hierarchical bismuth vanadate photoanode comodified with cobalt-iron prussian blue analogue and nickel-oxhydroxide for efficient solar water oxidation, Int. J. Hydrog. Energy 166 (2025) 150972.
[44] L. Shuai, Q. Li, X. Li, J. Wu, X. Huang, J. Yu, J. Dou, H. Li, X. Chen, Europium-doped amorphous iron oxyhydroxide ultra-thin nanolayer: a novel architecture for enhancing solar water splitting of bismuth vanadate photoanodes, J. Colloid Interface Sci. (2025) 138940.